Energy Storage Materials 63 (2023) 103048

Contents lists available at ScienceDirect

Energy Storage Materials

journal homepage: www.elsevier.com/locate/ensm

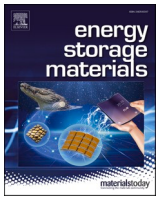

Chiolite $Na_5Ti_3F_{14}$: A novel sodium titanium fluoride anode for low-cost and high-performance Na-ion batteries

Jungmin Kang [a,b], Jinho Ahn [a,b], Yongseok Lee [a,b], Hyunyoung Park [a,b], Wonseok Ko [a,b], Bonyoung Ku [a,b], Myungeun Choi [a,b], Hun-Gi Jung [a,d,e], Won-Hee Ryu [c,*], Jongsoon Kim [a,b,d,e,**]

[a] Department of Energy Science, Sungkyunkwan University, Suwon 16419, Republic of Korea
[b] SKKU Institute of Energy Science and Technology, Sungkyunkwan University, Suwon 16419, Republic of Korea
[c] Department of Chemical and Biological Engineering, Sookmyung Women's University, 100 Cheongpa-ro 47-gil, Yongsan-gu, Seoul 04310, Republic of Korea
[d] KIST-SKKU Carbon-Neutral Research Center, Sungkyunkwan University, Suwon 16419, Republic of Korea
[e] Energy Storage Research Center, Korea Institution of Science and Technology, Seoul 02792, Republic of Korea

ARTICLE INFO

Keywords:
Na-ion batteries
$Na_5Ti_3F_{14}$
anode
Conversion reaction
Fluoride

ABSTRACT

Fluoride-based conversion reaction electrode materials offer exceptional theoretical capacity merit for Na-ion batteries. Nevertheless, it has rarely been considered as potential anode material candidate due to (i) excessive redox potential (> 3 V) and (ii) intrinsically low reaction kinetics related to sluggish structural reorganization process. In this work, we demonstrate that chiolite $Na_5Ti_3F_{14}$/carbon nanocomposite can deliver the outstanding electrochemical performances as the promising anode for Na-ion batteries, such as a large specific capacity of ~425 mAh g^{-1} at 10 mA g^{-1} with a low average operating voltage, the capacity retention of ~78 % compared to the initial capacity after 300 cycle with a high Coulombic efficiency of above 99 %, *etc*. We demonstrate that the chiolite $Na_5Ti_3F_{14}$ phase can store the ~8.33 mol Na ions through the following conversion reaction; $Na_5Ti_3F_{14} + 9Na + 9e^- \Leftrightarrow 3Ti + 14NaF$, which is clearly confirmed by various *ex-situ* analyses using X-ray diffraction, synchrotron-based X-ray adsorption spectroscopy, *etc*. We expect that this research can provide guidance toward the development of a new class of low-cost and high-performance anode materials, not only for Na-ion batteries but also for other rechargeable batteries.

1. Introduction

Indiscriminate use of fossil fuels causes the severe environmental problems such as air pollution [1]. Many car makers have attempted to develop electric vehicles (EVs) that utilize electricity as their energy source, rather than relying on gasoline or diesel. For efficient storage and usage of electricity, it is very important to apply the outstanding energy storage systems (ESSs), thus, lithium-ion batteries (LIBs) have great attention as the promising ESS for EVs because of their high energy densities and great electrochemical performances [2]. With the explosive growth in demands on the LIBs in the worldwide, however, the price of LIBs is rapidly increasing due to the small and concentrated sources of Li on earth. This makes it difficult to expand the application fields of LIBs to large-scale ESSs. It has been emphasized to develop the low-cost rechargeable batteries as the alternative to LIBs.

Recently, sodium-ion batteries (SIBs) have great attention as the promising low-cost rechargeable batteries, due to the unlimited Na sources in the sea and the alkali-ion-based reaction mechanisms similar with LIBs [3,4]. However, larger ionic size of Na^+ (~1.02 Å) than that of Li^+ (~0.76 Å) leads to the poor electrochemical behaviors of SIBs by sluggish Na^+ diffusion kinetics and large structural change during charge/discharge compared to those of LIBs [5]. Thus, it is important to develop the outstanding active materials for exhibiting the stable and reasonable electrochemical performances of the SIBs. Especially, it is known that graphite-based anode materials can only store a limited amount of Na^+ ions (~150 mAh g^{-1}) through a co-intercalation process [6]. The co-intercalation refers to the insertion of solvated alkali ions through the reduction of graphite [7] and was reported as a means to address the size mismatch between sodium ions and the graphene lattice. To increase the available capacity of anode materials for SIBs, many researchers have studied the various conversion-based materials, such as oxide, sulfide, fluoride, *etc*., with the high theoretical capacities based

* Corresponding author.
** Corresponding author at: Department of Energy Science, Sungkyunkwan University, Suwon 16419, Republic of Korea.
E-mail addresses: whryu@sookmyung.ac.kr (W.-H. Ryu), jongsoonkim@skku.edu (J. Kim).

https://doi.org/10.1016/j.ensm.2023.103048
Received 9 August 2023; Received in revised form 24 October 2023; Accepted 4 November 2023
Available online 5 November 2023

on the more than 1 mol electron transfer per 1 mol transition metal ions [8–10]. However, the intrinsic problems of the conversion-type anode materials, such as poor electrochemical properties and large volume expansion, still exist due to the sluggish kinetics [11]. These problem should be solved for real application of the conversion-type anode materials to SIBs. Metal fluorides, especially, are known for their low electronic conductivity and large band-gap energies, which make the facile conversion reaction with alkali ions difficult, leading to rapid capacity degradation [12]. Moreover, owing to high operating voltages (> 3 V) due to the highest electronegativity of fluorine, various fluoride materials have been just reported as the cathode material rather than the anode materials [13,14].

In this study, we introduce a novel Ti-based fluoride material, chiolite $Na_5Ti_3F_{14}$ as a promising anode material for SIBs. Through the conversion reaction between NaF and metallic Ti^0, $Na_5Ti_3F_{14}$ can deliver the large theoretical capacity of ~459 mAh g^{-1} corresponding to 9 mol Na^+ can totally be stored in the $Na_5Ti_3F_{14}$ phase. Using first-principles calculation and bond-valence energy landscape (BVEL) analyses, we demonstrated the $Na_5Ti_3F_{14}$ exhibits not only lower band-gap energy than other fluoride materials but also large three-dimensional Na^+ diffusion pathways, implying high electronic conductivity and facile Na^+ insertion for smooth conversion reaction in the $Na_5Ti_3F_{14}$ structure. Moreover, we performed the carbon-mixing process of the $Na_5Ti_3F_{14}$ for not only improvement of electrical conductivity but also provision of the buffer-layer to prevent large volume change during the conversion reaction. At the current density of 10 mA g^{-1}, the $Na_5Ti_3F_{14}$/carbon (NTF/C) nanocomposite delivered the large specific capacity of ~425 mAh g^{-1} with the low average voltage (*vs.* Na^+/Na), which is close to the theoretical capacity. Even at 1000 mA g^{-1}, its capacity was close to ~255 mAh g^{-1}. Furthermore, for 300 cycles at 1000 mA g^{-1}, the NTF/C nanocomposite exhibited the capacity retention of ~78 % compared with the initial capacity with a high coulombic efficiency of above 99 %. These outstanding power-capability and cyclability were achieved by not only reversible occurrence of facile conversion reaction under the SIB system but also existence of buffer layer by carbon-mixing. In addition, the reaction mechanism of $Na_5Ti_3F_{14}$ (conversion reaction: $Na_5Ti_3F_{14} + 9Na + 9e^- \Leftrightarrow 3Ti + 14NaF$) was confirmed during charge/discharge through various analyses, including *operando/ex-situ* X-ray diffraction (XRD), high-resolution transmission electron microscopy (HRTEM), *ex-situ* X-ray absorption near edge structure (XANES) analysis, and *ex-situ* X-ray photoelectron spectroscopy (XPS). Our findings will expand the research area of fluorine-based materials from cathode to anode and also provide insights for developing SIBs with outstanding electrochemical properties.

2. Material and methods

2.1. Synthesis of chiolite $Na_5Ti_3F_{14}$

Chiolite $Na_5Ti_3F_{14}$ powder was synthesized using NaF (Alfa Aesar, 99 %), and TiF_3 (Sigma Aldrich, 99 %) as precursors in a molar ratio of 5:3. To prevent water contamination, the precursors were sealed in a silicon nitride jar in the Ar-filled glove box and mixed using a high-energy ball milling at 400 rpm for 12 h. The mixture was calcined at 600 °C for 30 min under Ar flow. In addition, when pyromellitic acid is mixed and heat-treated during the synthesis process, the particles of the materials can be coated with carbon, which results in the improved electrical conductivity [15,16]. Thus, to enhance the electrical conductivity and the electrochemical performances, 10 wt% pyromellitic acid (PA, $C_6H_{10}O_2$) (Alfa Aesar, 96 %) precursor was mixed with the powder and sintered at 600 °C for 2 h under Ar flow. To improve electrical conductivity, an NTF/C nanocomposite was prepared by mixing the active material of $Na_5Ti_3F_{14}$ with conductive carbon (Super P Carbon black and multiwalled carbon nanotube) using a high-energy ball milling process at 300 rpm for 12 h. Through thermogravimetric analysis (TGA), it was verified that the weight loss of the $Na_5Ti_3F_{14}$/C nanocomposite in the temperature range of 40–600 °C was ~20 wt%, which means the amounts of the carbon in the $Na_5Ti_3F_{14}$/C nanocomposite. (Fig. S1).

2.2. Materials characterization

The as-prepared $Na_5Ti_3F_{14}$ powder and NTF/C nanocomposite were analyzed using XRD (PANalytical, Empyrean) with Mo Kα radiation (λ = 0.70932 Å). The step size was 0.13° and the 2θ range of 4.6° to 35.0°, and the patterns were converted to angles with Cu Kα radiation (λ = 1.54178 Å). The Rietveld refinement of the XRD data was performed using FullProf software. TGA was conducted under an air atmosphere at a heating rate of 10 °C min^{-1} using a thermogravimetric analyzer (Discovery TGA, USA) to 600 °C. The atomic ratios of elements, such as Na, Ti, were analyzed using an inductively coupled plasma-Atomic Emission Spectrometer (ICP-AES) installed at the National Center for Inter-university Research Facilities (NCIRF) at Seoul National University. The Brunauer-Emmett-Teller (BET) and Barrett-Joyner-Halenda (BJH) (ASAP2460M, USA) method were used to calculate the surface areas and average pore sizes. The valence states of Ti in the $Na_5Ti_3F_{14}$ structure were determined from XANES analysis performed on beamline 6D and 7D at the Pohang Accelerator Laboratory (PAL), South Korea. The Ti K-edge spectra were collected in the transmission mode with an electron energy of 2.5 GeV and a current of 200 mA. Ti reference spectra were simultaneously obtained from Ti metal foil. The particle size and distribution measurements were performed using FE-SEM (JEOL, JSM-7600) and high-resolution TEM (JEM-ARM200CF). The *operando* XRD (*o*-XRD) patterns of $Na_5Ti_3F_{14}$ were obtained using an X-ray diffractometer (PANalytical, Empyrean) with Mo Kα radiation λ = 0.7093 Å in the 2*θ* range from 10.0° to 19.0° with a step size of 0.01° Then, the patterns were converted to angles to Cu Kα radiation (λ = 1.54178 Å). The *Operando* XRD experiments were conducted using an *Operando* XRD battery cell (ISBS) made by PANalytical with PDC TECH. To protect the cell system from water, beryllium (Be) window was applied.

2.3. Electrochemical characterization

The NTF/C electrode was fabricated by mixing the 87.5 wt% NTF/C nanocomposite, 2.5 wt% Super P carbon black and 10 wt% polyvinylidene fluoride (PVDF) using *N*-methyl-2-pyrrolidone (NMP) as the solvent. Thus, the total weight percent of the NTF/C electrode was as follows; 70 wt% $Na_5Ti_3F_{14}$, 20 wt% conductive carbons and 10 wt% PVDF binder. The slurry was applied onto Cu foil using a doctor blade and dried at 100 °C for 3 h under vacuum condition. The mass loading of the electrode was ~2 mg cm^{-2}. CR2032 cells were prepared using the $Na_5Ti_3F_{14}$ electrode, Na metal as the counter electrode, a separator (Whatman GF/F glass fiber), and an electrolyte (1.0 M $NaPF_6$ in diethylene glycol dimethyl ether (DEGDME)). The coin cells were fabricated in an Ar-filled glove box. Galvanostatic charge/discharge tests were performed at various c-rates (10 mA g^{-1}, 20 mA g^{-1}, 40 mA g^{-1}, 60 mA g^{-1}, 120 mA g^{-1}, 240 mA g^{-1}, 360 mA g^{-1}, 480 mA g^{-1}, 600 mA g^{-1}, and 1000 mA g^{-1}) in the range of 0.01–3.0 V, using an automatic battery charge/discharge test system (WBCS 3000, WonATech).

2.4. Computational details

All the density functional theory (DFT) calculations were performed using the Vienna *Ab initio* Simulation Package (VASP) [17]. Projector-augmented wave (PAW) pseudopotentials [18] were used with a plane-wave basis set as implemented in VASP. Perdew–Burke–Ernzerhof (PBE) parametrization of the generalized gradient approximation (GGA) [19] was used for the exchange-correlation functional. A kinetic energy cutoff of 500 eV was used in all calculations, and all structures were optimized until the force in the unit cell converged to within 0.03 eV $Å^{-1}$. The GGA+*U* [20] method was adopted to address the localization of the d-orbital in Ti and

Fe ions, with U_{eff} values of 2.4, 5.0 eV, respectively as used in previous studies [21–23].

3. Result and discussion

3.1. Structural and morphological characterization of NTF/C nanocomposite

To investigate the detailed structure information of chiolite $Na_5Ti_3F_{14}$ phase in the NTF/C nanocomposite, we performed Rietveld refinement based on XRD patterns (Fig. 1a). It was confirmed that $Na_5Ti_3F_{14}$ was composed of $P4_22_12$ space group and was observed without any impurities and second phases [24]. The calculated lattice parameters of $Na_5Ti_3F_{14}$ were determined to be $a = b = 7.4504(3)$ Å and $c = 10.2383(7)$ Å with the low values of reliable factors ($R_P = 2.41\%$, $R_I = 3.47$ %, $R_F = 2.98\%$, and $\chi^2 = 5.80\%$), which indicate the high accuracy of the Rietveld refinement results [25]. Detailed structural information was provided such as the atomic positions, B_{iso}values, and

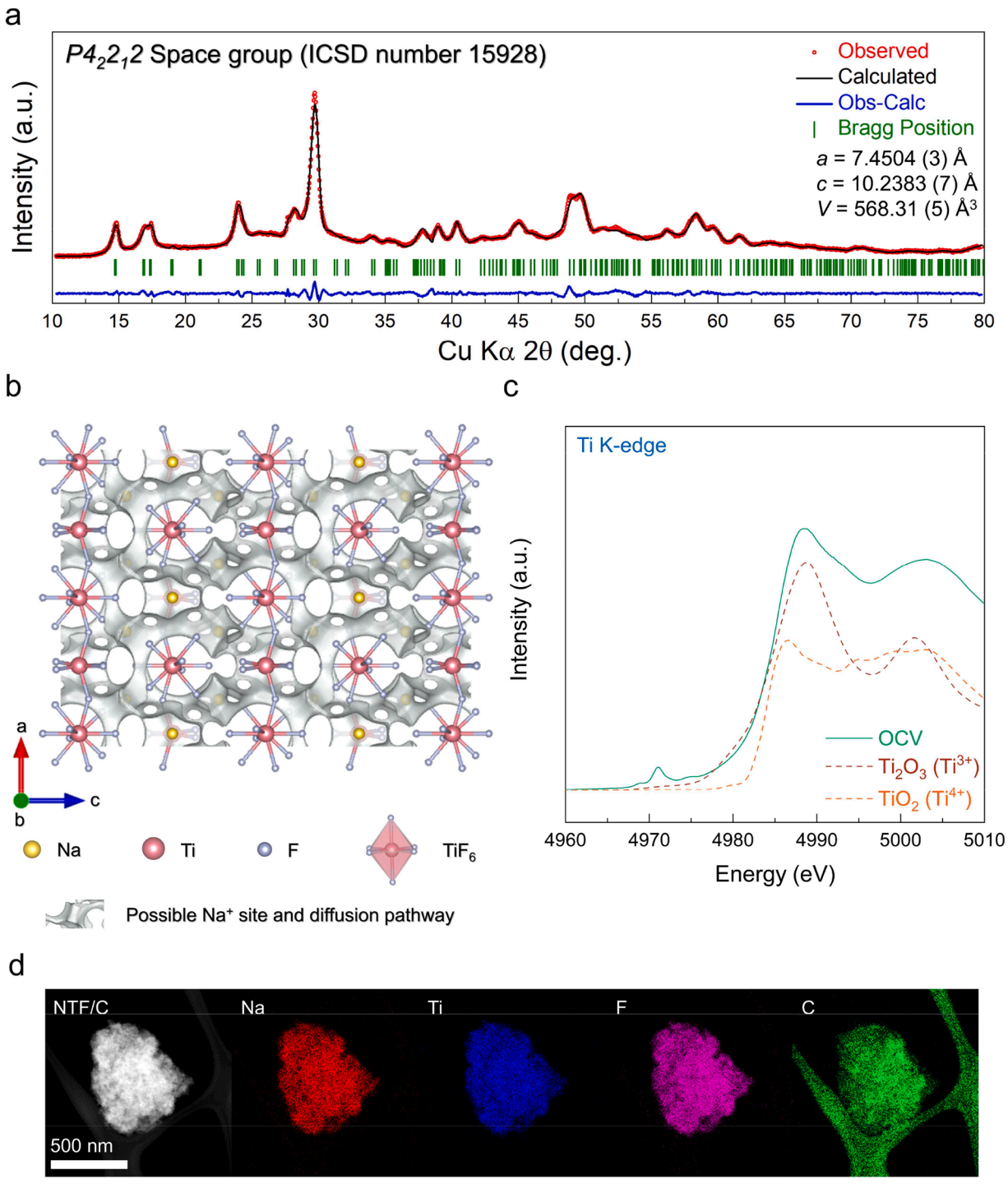

Fig. 1. Structural and morphological characterization of $Na_5Ti_3F_{14}$ phase in the NTF/C nanocomposite. (a) Refined XRD pattern of $Na_5Ti_3F_{14}$ phase in the NTF/C nanocomposite (ICSD number 15,928). (b) Three-dimensional (*ac* plane) BVEL analyses of $Na_5Ti_3F_{14}$ phase in the NTF/C nanocomposite with all Na^+ diffusion pathways in the crystal structure. (c) Ti K-edge XANES analysis of $Na_5Ti_3F_{14}$ phase in the NTF/C nanocomposite. (d) TEM-based EDS-mapping results of the NTF/C with Na, Ti, F, and C elements.

occupancies in Table S1. Based on the structural information, we determined the crystal planes of $Na_5Ti_3F_{14}$ structure. Moreover, we compared the XRD patterns of the as-prepared $Na_5Ti_3F_{14}$ and the NTF/C nanocomposite. As shown in Fig. S2 (Supporting Information), it was verified that the intensities of XRD peaks in the NTF/C nanocomposite were smaller than those in the as-prepared $Na_5Ti_3F_{14}$. Using Scherrer equation, we calculated the crystallite size of the as-prepared $Na_5Ti_3F_{14}$ and the NTF/C nanocomposite based on the XRD patterns (Table S2). These results imply a lowered particle size of the NTF/C nanocomposite after the carbon-mixing process using high-energy ball-milling. In addition, we performed the bond-valence energy landscape (BVEL) analysis to verify the possible Na^+ diffusion pathways in the structure. The BVEL method is a technique that estimates energy barriers and mechanisms associated with ion diffusion within a crystal structure using the bond valence site energy approach. The BVEL obtained through these calculations represents the energy landscape for the mobile ion, ultimately allowing for the prediction of pathways through which Na^+ can diffuse within the crystal structure [26,27]. As shown in Fig. 1b, it was verified that all the TiF_6 octahedra in the structure are three-dimensionally interconnected with each other and there are large Na^+ diffusion pathways in the structure, which implies facile Na^+ diffusion can be possible in the crystal structure of $Na_5Ti_3F_{14}$ phase. The large Na^+ diffusion pathway of the $Na_5Ti_3F_{14}$ phase can facilitate intercalation reaction deeply inside at the beginning of discharge, thereby enabling subsequent conversion reaction in lower voltage range for discharge by formation of intimate Na-F clusters [28]. Moreover, to confirm the oxidation state of Ti cations on the NTF/C nanocomposite, we performed the X-ray absorption near edge structure (XANES) analyses (Fig. 1c). It was verified that the Ti K-edge XANES spectrum of the NTF/C nanocomposite was similar to that of $Ti_2^{(3+)}O_3$ rather than $Ti^{(4+)}O_2$, indicating that the average oxidation state of Ti ions in the NTF/C was close to +3.

Through scanning electron microscope (SEM) analyses (Fig. S3), it was verified that the morphologies of both $Na_5Ti_3F_{14}$ and $Na_5Ti_3F_{14}$/C anode materials are uniform. In addition, it was confirmed that the particle size of $Na_5Ti_3F_{14}$/C is smaller than as-prepared $Na_5Ti_3F_{14}$. Moreover, the particle size and atomic distribution of the NTF/C nanocomposite was investigated through the transmission electron microscopy (TEM) and energy-dispersive X-ray spectroscopy (EDS) analyses. As shown in Fig. 1d, it was revealed that Na, Ti, F and C elements were homogeneously distributed in the particles with ~600 nm, indicating the well carbon-coating on the NTF/C particles. The total elemental ratio of Na and Ti in the NTF/C nanocomposite was ~5.000:2.998. The atomic ratio in the NTF/C nanocomposite was in good agreement with the inductively coupled plasma atomic emission spectroscopy (ICP-AES) analysis (Table S3). In addition, the Brunauer-Emmett-Teller (BET) and Barrett-Joyner-Halenda (BJH) analyses indicated that the surface area and the average pore size of the NTF/C nanocomposite are ~56.4585 $m^2\ g^{-1}$ and ~32.0907 nm, respectively (Fig. S4), which are larger than those of the as-prepared $Na_5Ti_3F_{14}$ (= ball-milled $Na_5Ti_3F_{14}$) and the $Na_5Ti_3F_{14}$ without ball-milling (Figs. S5 and S6). Moreover, the surface area and average pore size of the carbon are also ~67.3709 $m^2\ g^{-1}$ and ~29.8826 nm, respectively (Fig. S7). Furthermore, the surface area and average pore size of the NTF/C nanocomposite after charging to 3.0 V (*vs.* Na^+/Na) were approximately ~55.9879 $m^2\ g^{-1}$ and ~31.5352 nm, respectively, which is closely similar to those of the OCV-state NTF/C nanocomposite (Fig. S8). On the other hand, in the case of the as-prepared $Na_5Ti_3F_{14}$, the surface area and average pore size after charging to 3.0 V were confirmed to be approximately ~12.4360 $m^2\ g^{-1}$ and ~25.1114 nm, respectively (Fig. S9), which is much larger than those of the OCV-state as-prepared $Na_5Ti_3F_{14}$. These results imply that the reversible feature of the average surface area and pore size in the NTF/C nanocomposites during charge/discharge can result in the improved electrochemical performances. Carbon exhibits a high affinity for adsorbing molecules on its surface. Consequently, when carbon is mixed with a material, it can create additional adsorption sites, resulting in an increase in surface area. Moreover, owing to carbon coating through the high-energy ball-milling process, the particle sizes of NTF/C nanocomposite became smaller than those of the as-prepared $Na_5Ti_3F_{14}$, which indicates the increased specific surface area of NTF/C nanocomposite compared to as-prepared $Na_5Ti_3F_{14}$. The increased surface area by the decreased particle size was also reported in the previous research paper [29]. In addition, during the carbon-mixing process, carbon particles may agglomerate or cluster together. These aggregates can occupy the spaces between the particles in $Na_5Ti_3F_{14}$/C nanocomposite, leading to the formation of larger interconnected pores. Thus, the carbon-mixing can result in increase of the average pore size in the $Na_5Ti_3F_{14}$/C nanocomposite. Through BET and BJH analyses, it was verified that NTF/C show an increase in both surface area and pore size compared to as-prepared $Na_5Ti_3F_{14}$, which indicates that the increase in interfacial contact area between the electrode and the electrolyte allows for efficient kinetic and ion transfer of the material, ultimately indicating an enhancement in electrochemical properties. These results are also well matched with the various previous reports [30–32].

3.2. Outstanding electrochemical performances of NTF/C nanocomposite as an anode of SIBs

The power-capability of the NTF/C nanocomposite was investigated through electrochemical tests at the various current densities in the voltage range of 0.01–3.0 V (*vs.* Na^+/Na) after the initial discharge. The initial discharge capacity was ~689 mAh g^{-1}, which was attributed not only to the conversion reaction between $Na_5Ti_3F_{14}$ and Na, but also to the occurrence of side reactions due to the formation of a solid-electrolyte-interphase (SEI) layer (Fig. S10) [33]. The large initial discharge capacity of the NTF/C nanocomposite by formation of SEI layer is similar with those of other conversion-based anode materials [34,35]. As shown in Fig. 2a, b, the NTF/C nanocomposite delivered a large specific capacity of ~425 mAh g^{-1} at 10 mA g^{-1} (1C = 459 mA g^{-1}) after the pre-cycling process, corresponding to the storage of ~8.33 mol Na^+ during charge/discharge. This result implies the $Na_5Ti_3F_{14}$ phase in the nanocomposite experienced the following conversion reaction; $Na_5Ti_3F_{14} + 9Na^+ + 9e^- \Leftrightarrow 3Ti + 14NaF$. Even at the high current density of 1000 mA g^{-1}, in particular, the specific capacity was maintained up to ~255 mAh g^{-1} corresponding to ~60 % of the capacity measured at 10 mA g^{-1}, which indicates the outstanding power-capability of the NTF/C nanocomposite. It means that the wide Na ion channel of NTF/C with a three-dimensional structure allows facile Na^+ insertion into the structure, providing enough opportunity to create the Na-F phase during the conversion reaction after the initial intercalation process, resulting in excellent properties. In addition, we tested the electrochemical tests of the as-prepared $Na_5Ti_3F_{14}$ and the NTF/C nanocomposite in the various current densities from 10 mA g^{-1} to 1000 mA g^{-1} with the same conditions under the SIB system. As shown in Fig. S11, it was clearly verified that the $Na_5Ti_3F_{14}$/C nanocomposite exhibited better power-capability than the as-prepared $Na_5Ti_3F_{14}$ and $Na_5Ti_3F_{14}$ without ball-milling. Moreover, we performed the electrochemical performances of NTF/C with more increased mass loading (~6 mg cm^{-2}). As shown in Fig. S12, it was verified that the NTF/C with mass loading of ~6 mg cm^{-2} delivered outstanding electrochemical performances. These results mean the kinetics of the conversion reaction on the $Na_5Ti_3F_{14}$ under the SIB system was successfully enhanced by synergy of carbon-mixing and nano-sizing. As shown in the Fig. S13, electrochemical impedance spectroscopy (EIS) analysis was performed to compare the diffusion kinetics of the NTF/C nanocomposite. It was verified that the charge-transfer resistance of NTF/C half-cell was ~321 Ω. Moreover, we performed an electrochemical property test to confirm that Na ions are extracted from $Na_5Ti_3F_{14}$ during the charge process (Fig. S14). The charge capacity of NTF/C was delivered just ~ 0.4 mAh g^{-1}, indicating that Na ions in the $Na_5Ti_3F_{14}$ phase in NTF/C are negligibly extracted during the charging

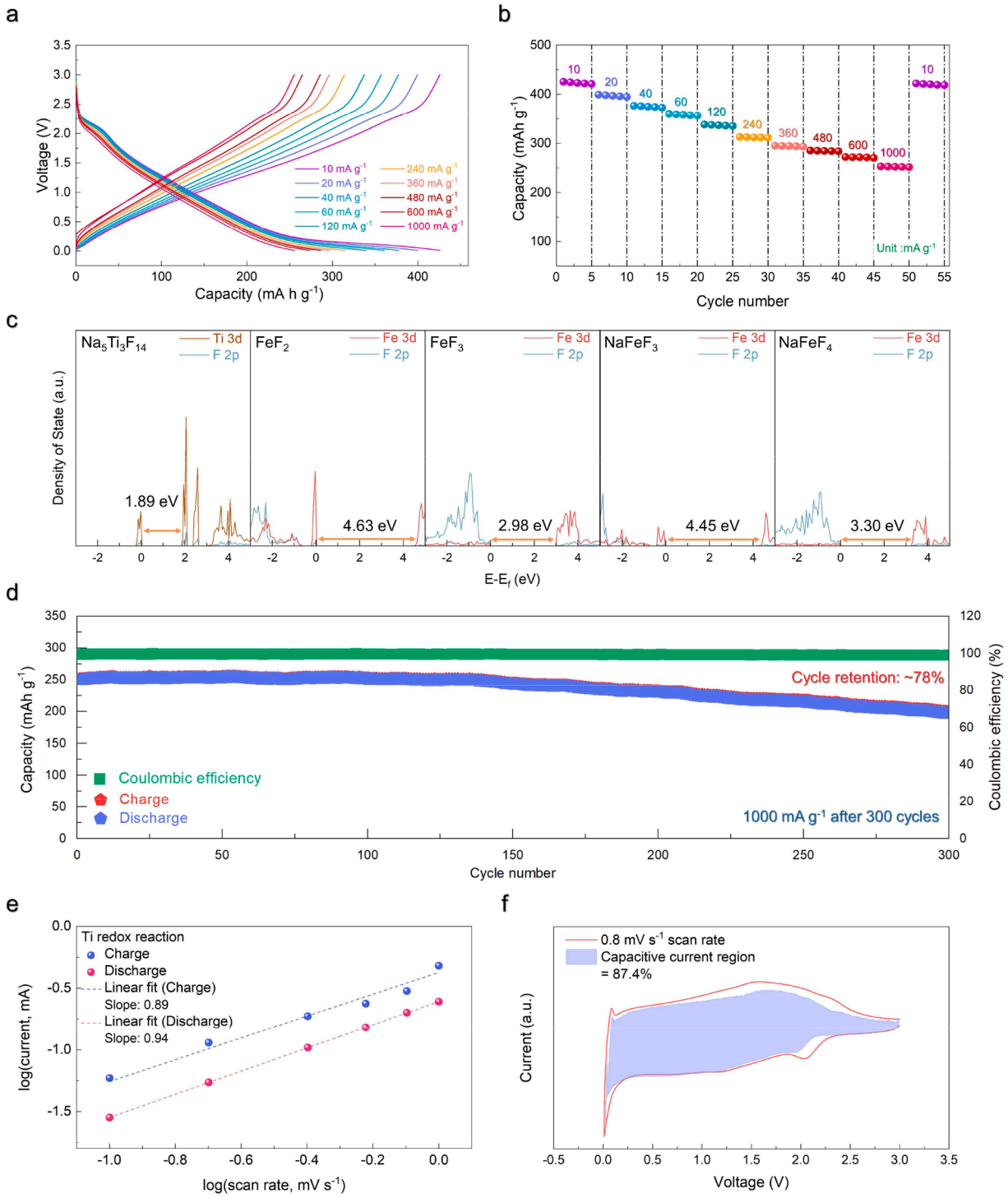

Fig. 2. Electrochemical performance with high power and long-term cycle stability of NTF/C. (a) Charge/discharge profiles of NTF/C in the range of 0.01–3.0 V at various current rates. (b) Power-capability of NTF/C with several cycles at various current rates. (c) pDOS of Fe 3d and Ti 3d of various fluoride-based materials for Na-ion batteries. (d) Cycle performance of NTF/C at 1000 mA g^{-1} for 300 cycles in the voltage range of 0.01–3.0 V (*vs.* Na^{+}/Na). (e) Log(*i*) and log(*v*) plots on Ti ions redox reactions at specific peak currents. (f) CV profiles with the calculated pseudo capacitance shaded region at 0.8 mV s^{-1} during the charge/discharge.

process. In addition, we investigated the theoretical density of state (DOS) of $Na_5Ti_3F_{14}$ to verify the intrinsic electronic conductivity using first-principles calculation, and then, compared it with other fluoride-based materials. As shown in Fig. 2c, it was revealed that $Na_5Ti_3F_{14}$ has lower band gap energy (~1.89 eV) than other fluoride-based materials, which also supports the outstanding power-capability of the NTF/C nanocomposite despite the fluoride-based conversion reaction. Moreover, the various information and characteristics of fluoride-based materials for NIBs were summarized in Table S4 [3,21,36–38]. It was verified that the band gap energies of $Na_5Ti_3F_{14}$ and $Na_2Fe_2F_7$ are lower than those of other fluoride-based materials. This result indicates that the crystal structure of $Na_5Ti_3F_{14}$ enables the high electronic conductivity, resulting in the outstanding power-capability as the promising anode for SIBs. Furthermore, the NTF/C nanocomposite exhibited the outstanding capacity retention of ~78 % compared with a high Coulombic efficiency of

above 99 % after 300 cycles at 1000 mA g^{-1} (Fig. 2d).

To confirm the possibility of the NTF/C nanocomposite as the promising anode for SIBs, in addition, we also performed the full-cell test using $Na_{0.67}[Mn_{0.8}Ni_{0.1}Co_{0.1}]O_2$ (NaMNC) as the cathode with N/P ratio of ~1.2. Fig. S15 shows that the NaMNC at the current density of 26 mA g^{-1} under the half-cell test exhibited the discharge capacity of ~165 mAh g^{-1}. Before the full-cell test, the NTF/C nanocomposite was pre-cycled in the range of 0.01–3.0 V (*vs.* Na^+/Na) to eliminate the irreversible capacity. By using NTF/C as the anode, it appears that electrochemical properties of the NaMNC||NTF/C full-cell was conducted in a lower voltage range due to the higher operating voltage compared to hard carbon [39]. At the current density of 26 mA g^{-1}, the NaMNC||NTF/C full-cell delivered the specific capacity of ~164 mAh g^{-1} in the voltage range of 0.7–3.6 V (Fig. S16). Furthermore, it was revealed that the NaMNC||NTF/C full-cell exhibited the great cycle performance with capacity retention of ~70% compared to initial capacity for 400 cycles at the current density of 120 mA g^{-1} and the Coulombic efficiency was above 99 %. In addition, we analyzed the differential capacity *versus* voltage (*dQ/dV*) plots of NaMNC||NTF/C full-cell in various cycle conditions. (Fig. S17). In the high voltage region near 3.6 V, no significant peak corresponding to electrolyte decomposition was detected in the *dQ/dV* profiles, even after 400 cycles. This indicates the excellent electrochemical performances of the NaMNC||NTF/C full-cell and the electrolyte stability at the high voltage

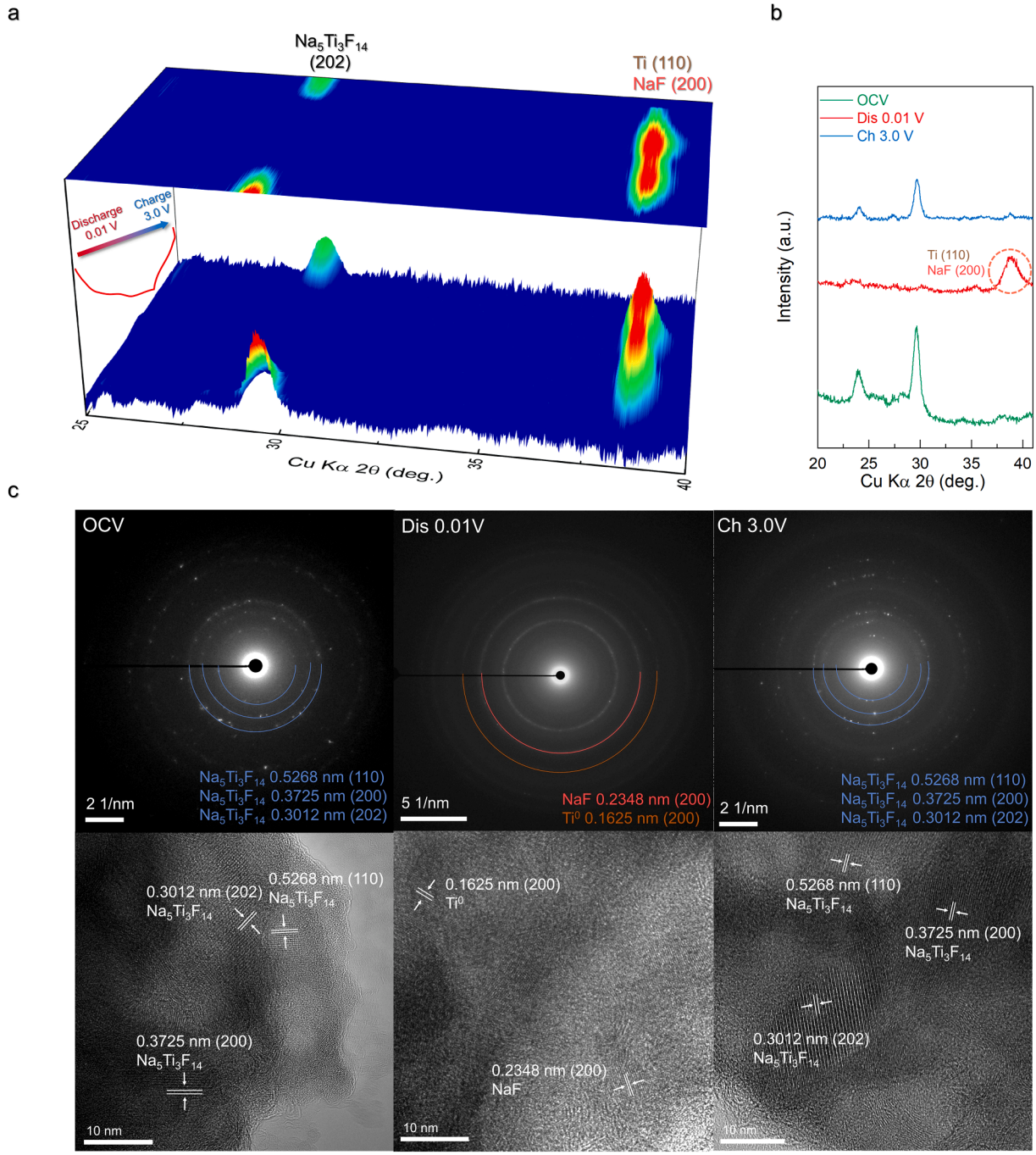

Fig. 3. Identify of structural change and reaction mechanism of NTF/C (a) *o*-XRD patterns of NTF/C with the upper part in 2D format and the lower part in 3D format measured at a current rate of 120 mA g^{-1} in the voltage range of 0.01–3.0 V (*vs.* Na^+/ Na). (b) *Ex-situ* XRD patterns of OCV, Dis 0.01 V, and Ch 3.0 V between 20° and 42° (c) HRTEM and SAED patterns of the OCV, Dis 0.01 V, and Ch 3.0 V of NTF/C.

of 3.6 V. In addition, we conducted the EIS analyses of the full-cell (Fig. S18). The charge-transfer resistance of the full cell was verified to be ~737 Ω. Moreover, the CV results of the full-cell show the reversible electrochemical reaction during charge/discharge (Fig. S19). Furthermore, the full-cell performance was also better cycle-performances than other layered-type cathode materials for SIBs, which demonstrates the applicability of the NTF/C nanocomposite anode material in SIBs (Fig. S20) [40–44]. We supposed that the

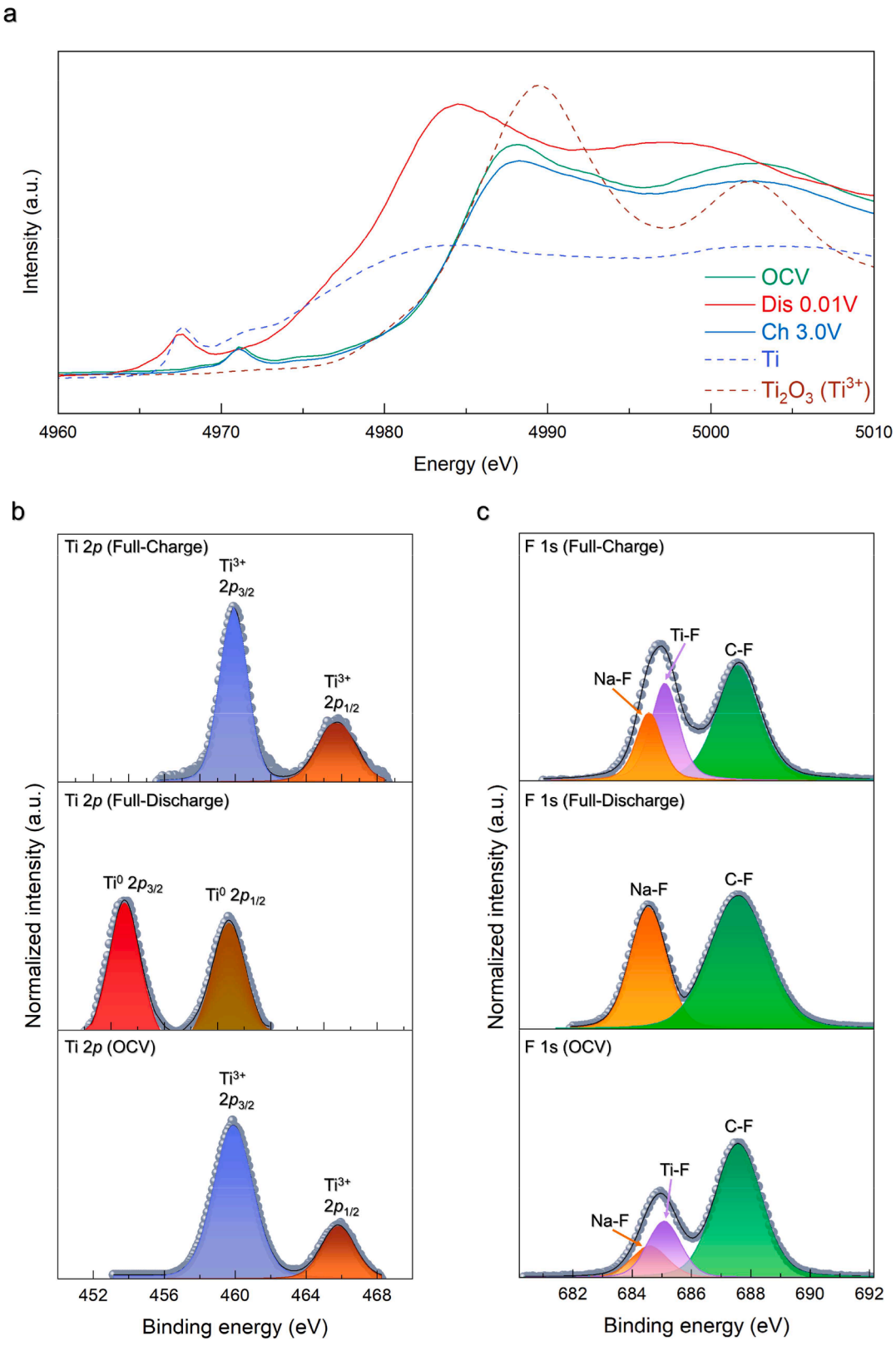

Fig. 4. Confirmation of redox reaction in NTF/C through XAFS and XPS analysis. *Ex-situ* (a) Ti XANES analyses of NTF/C electrode. *Ex-situ* XPS spectra of NTF/C electrode: (b) Ti 2p and (c) F 1 s peaks.

excellent cycle performance was due to highly reversible conversion reaction during charge/discharge.

In addition, the cyclic voltammetry (CV) analysis was performed at the various scan rates to confirm the Na^+ storage ability and contribution of pseudo-capacitance. It showed that the broad peak observed in the first cycle at ~0.5 V corresponds to the formation of the SEI layer, and it was not observed after severe cycles (Fig. S21a, b). It was verified that the broad redox peaks at ~1.2 V (anodic process) and ~1.5 V (cathodic process) are detected in the CV profiles, which indicates the electrochemical reaction of NTF/C under the SIB system. Based on the CV profiles, it was verified that the Na storage on the NTF/C nanocomposite during charge/discharge was mainly affected by surface-controlled reactions ($b \approx 0.89$ and 0.94 in the equation of $i_p = av^b$) (Fig. 2e). Moreover, we calculated the contribution of pseudo capacitance through the equation of $i(V)=k_1v+k_2v^{1/2}$. At a scan rate of 0.8 mV s^{-1} during charge/discharge, the contribution of the pseudo capacitance of the NTF/C nanocomposite was found to be ~87.4 %, which also indicates that most of the capacitance of the NTF/C nanocomposite was determined by the surface-controlled reaction (Fig. 2f).

3.3. Reaction mechanism of $Na_5Ti_3F_{14}$ phase in the NTF/C nanocomposite

To investigate the conversion reaction mechanism of $Na_5Ti_3F_{14}$ phase in the NTF/C nanocomposite occurred during charge/discharge, we performed the *operando* XRD (*o*-XRD) analyses (Fig. 3a). In OCV state, the (202) plane of $Na_5Ti_3F_{14}$ phase was observed at ~29.7° (2θ). During discharging to 0.01 V, the $Na_5Ti_3F_{14}$ phase gradually disappeared, and a new broadened XRD peak was detected at ~38.3° corresponding to the (110) plane of metallic Ti^0 and the (200) plane of NaF. During charging to 3.0 V, it was observed that the (202) plane gradually reappeared. These results from *o*-XRD were consistent with the *ex-situ* XRD pattern (Fig. 3b). Thus, through combined studies using *operando/ex-situ* XRD analyses, it was revealed that $Na_5Ti_3F_{14}$ phase in the NTF/C nanocomposite reversibly experience the following conversion reaction during charge/discharge; $Na_5Ti_3F_{14} + 9Na^+ + 9e^- \Leftrightarrow 3Ti + 14NaF$. Furthermore, the *ex-situ* HRTEM and selected-area electron diffraction (SAED) analyses were performed to confirm the reversible conversion reaction of $Na_5Ti_3F_{14}$ phase under the SIB system. As shown in Fig. 3c, it was verified that the OCV sample was composed of the $Na_5Ti_3F_{14}$ phase. After charging to 3.0 V, the $Na_5Ti_3F_{14}$ phase was

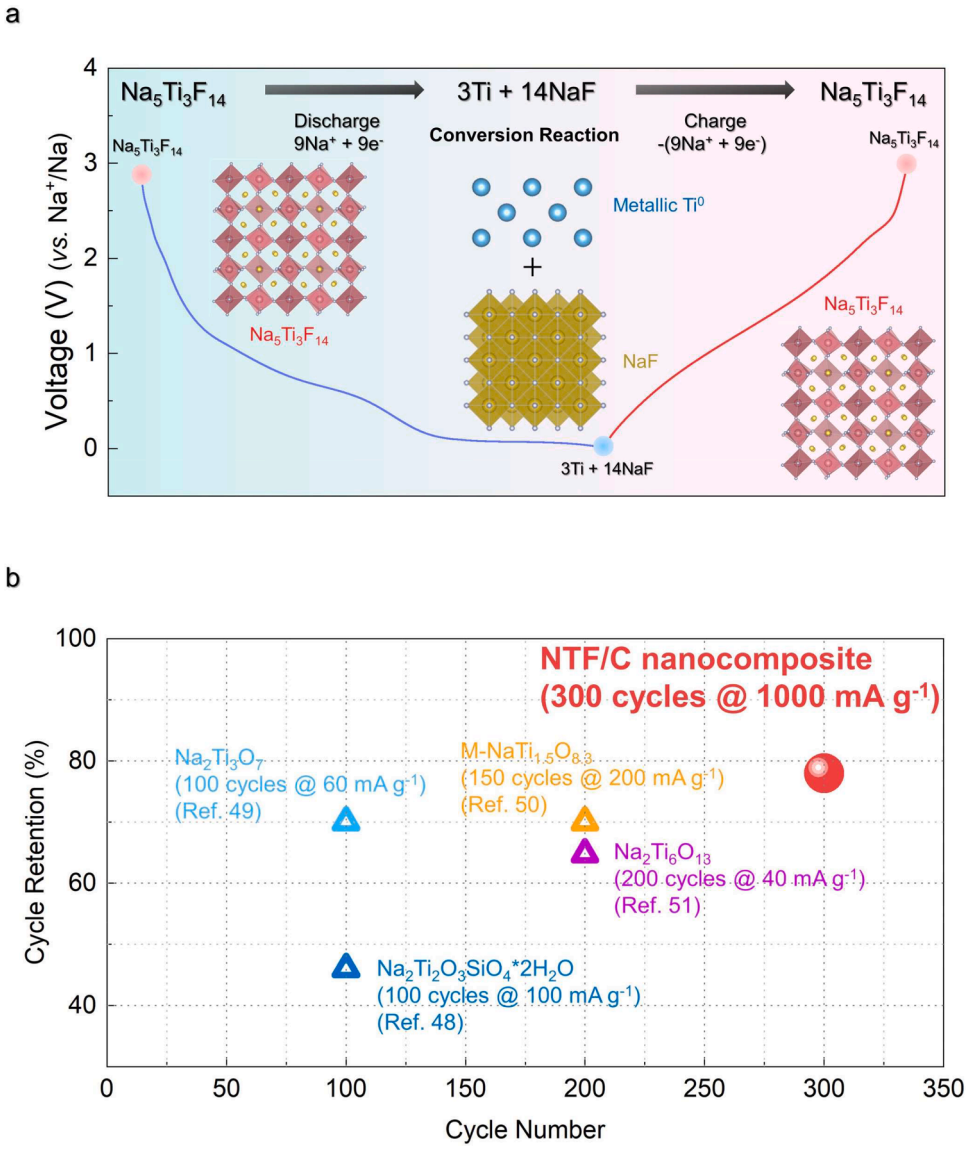

Fig. 5. (a) Schematic illustration of summarization for reaction mechanism of NTF/C on charge/discharge process. (b) Comparison of cycle-performances among NTF/C nanocomposite and other Ti-based anode materials for SIBs.

recovered in the reverse order. These results on the (*hkl*) plane and *d*-spacing of the $Na_5Ti_3F_{14}$, NaF and metallic Ti^0 phases are consistent with the *operando/ex-situ* XRD results.

The overall expected redox reaction mechanism of $Na_5Ti_3F_{14}$ was investigated by synchrotron-based *ex-situ* XANES to confirm the Ti-based conversion. As observed in Fig. 4a, the Ti K-edge spectra gradually shift to lower energy level during discharging to 0.01 V, indicating that the oxidation state of Ti changed from Ti^{3+} to metallic Ti^0. During charging to 3.0 V, the oxidation state of Ti was recovered to Ti^{3+}, which was similar to the OCV state. *Ex-situ* X-ray photoelectron spectroscopy (XPS) results also showed the reversible conversion reaction of $Na_5Ti_3F_{14}$ during charge/discharge. As presented in Fig. 4b, it was confirmed that the Ti^{3+} $2p_{3/2}$ peak (459.8 eV) and Ti^{3+} $2p_{1/2}$ peak (465.8 eV) disappeared during discharging to 0.01 V, and the metallic Ti^0 $2p_{3/2}$ peak (453.7 eV) and Ti^0 $2p_{1/2}$ peak (459.7 eV) were newly formed [45–47]. After charging to 3.0 V, the Ti^{3+} $2p_{3/2}$ peak and Ti^{3+} $2p_{1/2}$ peak were clearly detected, and the metallic Ti^0 signals were negligible. In terms of the F 1 s XPS spectra, it was also verified that the Ti-F bonds appeared and disappeared reversibly during charge/discharge, as shown in Fig. 4c. In addition, it was confirmed that even after 300 cycles, the XPS analysis results showed peak formation similar to that of the OCV state (Fig. S22). These *ex-situ* XPS results were consistent with the *ex-situ* XANES results. In addition, we illustrated the overall conversion-based reaction mechanism of $Na_5Ti_3F_{14}$ during charge/discharge (Fig. 5a), which shows $Na_5Ti_3F_{14}$ phase in the NTF/C nanocomposite can store the approximately 8.33 mol Na^+ corresponding to ~425 mAh g^{-1} through the following conversion reaction; $Na_5Ti_3F_{14} + 9Na + 9e^- \Leftrightarrow 3Ti + 14NaF$. This excellent cycle performance was also demonstrated by negligible morphological deformation in the NTF/C nanocomposites after 300 cycles (Fig. S23). Moreover, it was confirmed the NTF/C nanocomposite exhibited better cycle-performance and power-capability than other Ti-based anode materials for SIBs, which indicates the excellence of the NTF/C nanocomposite based on the stable and reversible conversion reaction as the promising anode for high-performance SIBs (Fig. 5b and S24) [48–51]. Furthermore, it was confirmed that the $Na_5Ti_3F_{14}$ phase in the NTF/C nanocomposite exhibited excellent electrochemical performance compared to previously report fluoride-based anode materials for SIBs. (Table S5) [52–55]. In addition, conversion-type materials have encountered issues such as voltage hysteresis, discharge profiles, rate stability, cyclic stability, irreversible capacity loss, and Coulombic efficiencies, and there have been no commercially reported cases. Thus, various research endeavors are underway to partially address these issues, and notably, potential solutions to overcome these drawbacks are being introduced through the following methods (i: Size control ii: Morphology control iii: Architectural control iv: Composite with carbon) [56–58]. By integrating each of these solutions, it is possible to enhance the electrochemical properties of conversion-type materials and achieve structural stability. This could serve as a means to advance the commercialization of conversion materials. Our findings suggest that the NTF/C nanocomposite can be applied as a promising and outstanding anode for low-cost and high-performance Na-ion batteries.

4. Conclusion

In this work, we demonstrated the successful conversion reaction of NTF/C nanocomposite as a novel fluoride-based anode material for SIBs with exceptional electrochemical performance. Charge conductivity and reaction kinetics were improved through conductive carbon coating and downsizing process, which effectively affected the stable structural properties of $Na_5Ti_3F_{14}$, having a three-dimensional open framework. The facile Na channel and deep Na intercalation inside particle can facilitate subsequent conversion reaction with higher molar number of Na^+ uptake (~8.33 mol Na^+). During charge/discharge at a current density of 10 mA g^{-1}, $Na_5Ti_3F_{14}$ delivered a specific capacity of ~425 mAh g^{-1}. Even at 1000 mA g^{-1}, a specific capacity of ~255 mAh g^{-1} was obtained, which retained up to 60% of the measured capacity at 10 mA g^{-1}. Through various *ex-situ* techniques such as XRD, HRTEM, XANES, and XPS analyses, it was clearly confirmed that the reversible conversion/deconversion reaction ($Na_5Ti_3F_{14} + 9Na + 9e^- \Leftrightarrow 3Ti + 14NaF$) occurs during charge/discharge of $Na_5Ti_3F_{14}$. Therefore, $Na_5Ti_3F_{14}$ demonstrates that despite the conversion reaction, the capacity retention was maintained at ~78 % for 300 cycles at 1000 mA g^{-1} with acceptable low operating voltage and high Coulombic efficiency of above 99 %. In addition, it is important to discover the optimal values of surface area, pore size and carbon contents, to satisfy both high tap density and facial Na^+ diffusion kinetics. Thus, the electrochemical performances of the NTF/C can be more enhanced through further modification. We raise the fact that fluoride-based materials can be introduced to conversion reaction anode materials and also offer their outstanding performance benefit as potential anode for beyond-Li batteries.

CRediT authorship contribution statement

Jungmin Kang: Validation, Visualization, Investigation, Methodology, Formal analysis, Writing – original draft. **Jinho Ahn:** Visualization, Investigation. **Yongseok Lee:** . **Hyunyoung Park:** Investigation, Methodology. **Wonseok Ko:** Validation, Methodology. **Bonyoung Ku:** Formal analysis, Visualization. **Myungeun Choi:** Validation, Methodology. **Hun-Gi Jung:** Formal analysis. **Won-Hee Ryu:** Conceptualization, Visualization, Formal analysis, Data curation, Writing – review & editing. **Jongsoon Kim:** Supervision, Project administration, Conceptualization, Visualization, Formal analysis, Data curation, Writing – review & editing.

Declaration of Competing Interest

The authors declare that they have no known competing financial interests or personal relationships that could have appeared to influence the work reported in this paper.

Data availability

Data will be made available on request.

Acknowledgement

This research was supported by the National Research Foundation of Korea funded by the Ministry of Science and ICT of Korea (NRF-2021R1A2C1014280). Also, this work was supported by the KIST Institutional Program (No. 2E32581–23–092).

Supplementary materials

Supplementary material associated with this article can be found, in the online version, at doi:10.1016/j.ensm.2023.103048.

References

[1] S. Akhtar, W. Lee, M. Kim, M.S. Park, W.S. Yoon, conduction mechanism of charge carriers in electrodes and design factors for the improvement of charge conduction in Li-ion batteries, J. Electrochem. Sci. Technol. 12 (2021) 1–20, https://doi.org/10.33961/jecst.2020.01564.

[2] B. Dunn, H. Kamath, J.M. Tarascon, Electrical energy storage for the grid: a battery of choices, Science 334 (80–) (2011) 928–935, https://doi.org/10.1126/science.1212741.

[3] H. Park, Y. Lee, M. Cho, J. Kang, W. Ko, Y.H. Jung, T. Jeon, J. Hong, H. Kim, S. T. Myung, J. Kim, $Na_2Fe_2F_7$: a fluoride-based cathode for high power and long life Na-ion batteries, Energy Environ. Sci. 14 (2021) 1469–1479, https://doi.org/10.1039/D0EE02803G.

[4] J. Kang, J. Ahn, H. Park, W. Ko, Y. Lee, S. Lee, S. Lee, S. Jung, J. Kim, Highly stable Fe^{2+}/Ti^{3+}-based fluoride cathode enabling low-cost and high-performance Na-Ion

batteries, Adv. Funct. Mater. 32 (2022), 2201816, https://doi.org/10.1002/adfm.202201816.
[5] J. Kang, H. Park, H. Kim, J.H. Jo, W. Ko, Y. Lee, S. Myung, J. Kim, Development of a new mixed-polyanion cathode with superior electrochemical performances for Na-ion batteries, ACS Sustain. Chem. Eng. 8 (2020) 163–171, https://doi.org/10.1021/acssuschemeng.9b04944.
[6] H. Kim, J. Hong, Y.U. Park, J. Kim, I. Hwang, K. Kang, Sodium storage behavior in natural graphite using ether-based electrolyte systems, Adv. Funct. Mater. 25 (2015) 534–541, https://doi.org/10.1002/adfm.201402984.
[7] B. Jache, P. Adelhelm, Use of graphite as a highly reversible electrode with superior cycle life for sodium-ion batteries by making use of Co-intercalation phenomena, Angew. Chemie Int. Ed. 53 (2014) 10169–10173, https://doi.org/10.1002/anie.201403734.
[8] D. Li, J. Zhou, X. Chen, H. Song, Amorphous Fe_2O_3/graphene composite nanosheets with enhanced electrochemical performance for sodium-ion battery, ACS Appl. Mater. Interfaces 8 (2016) 30899–30907, https://doi.org/10.1021/acsami.6b09444.
[9] Y. Li, J. Qian, M. Zhang, S. Wang, Z. Wang, M. Li, Y. Bai, Q. An, H. Xu, F. Wu, L. Mai, C. Wu, Co-construction of sulfur vacancies and heterojunctions in tungsten disulfide to induce fast electronic/ionic diffusion kinetics for sodium-ion batteries, Adv. Mater. 32 (2020), 2005802, https://doi.org/10.1002/adma.202005802.
[10] Y. Wei, X. Ma, X. Huang, B. Zhao, X. Zhu, C. Liang, Z. Zi, J. Dai, Solvothermal synthesis of porous MnF_2 hollow spheroids as anode materials for sodium-/lithium-ion batteries, ChemElectroChem 6 (2019) 2726–2732, https://doi.org/10.1002/celc.201900147.
[11] Y. Lee, J. Kang, J. Ahn, W. Ko, H. Park, S. Lee, S. Lee, J. Yoo, J. Kim, A high-energy conversion-type cathode activated by amorpholization for Li rechargeable batteries, J. Mater. Chem. A 10 (2022) 20080–20089, https://doi.org/10.1039/D2TA02167F.
[12] Y. Yamada, T. Doi, I. Tanaka, S. Okada, J. Yamaki, Liquid-phase synthesis of highly dispersed $NaFeF_3$ particles and their electrochemical properties for sodium-ion batteries, J. Power Sources 196 (2011) 4837–4841, https://doi.org/10.1016/j.jpowsour.2011.01.060.
[13] C. Li, C. Yin, X. Mu, J. Maier, Top-down synthesis of open framework fluoride for lithium and sodium batteries, Chem. Mater. 25 (2013) 962–969, https://doi.org/10.1021/cm304127c.
[14] S.K. Jung, I. Hwang, S.P. Cho, K. Oh, K. Ku, I.R. Choi, K. Kang, New iron-based intercalation host for lithium-ion batteries, Chem. Mater. 30 (2018) 1956–1964, https://doi.org/10.1021/acs.chemmater.7b05017.
[15] M.M. Doeff, J.D. Wilcox, R. Yu, A. Aumentado, M. Marcinek, R. Kostecki, Impact of carbon structure and morphology on the electrochemical performance of $LiFePO_4$/C composites, J. Solid State Electrochem. 12 (2008) 995–1001, https://doi.org/10.1007/s10008-007-0419-9.
[16] J.D. Wilcox, M.M. Doeff, M. Marcinek, R. Kostecki, Factors influencing the quality of carbon coatings on $LiFePO_4$, J. Electrochem. Soc. 154 (2007) A389, https://doi.org/10.1149/1.2667591.
[17] G. Kresse, J. Furthmüller, Efficiency of ab-initio total energy calculations for metals and semiconductors using a plane-wave basis set, Comput. Mater. Sci. 6 (1996) 15–50, https://doi.org/10.1016/0927-0256(96)00008-0.
[18] P.E. Blöchl, Projector augmented-wave method, Phys. Rev. B 50 (1994) 17953–17979, https://doi.org/10.1103/PhysRevB.50.17953.
[19] J.P. Perdew, K. Burke, M. Ernzerhof, Generalized gradient approximation made simple, Phys. Rev. Lett. 77 (1996) 3865–3868, https://doi.org/10.1103/PhysRevLett.77.3865.
[20] V.I. Anisimov, A.I. Poteryaev, M.A. Korotin, A.O. Anokhin, G. Kotliar, First-principles calculations of the electronic structure and spectra of strongly correlated systems: dynamical mean-field theory, J. Phys. Condens. Matter. 9 (1997) 7359–7367, https://doi.org/10.1088/0953-8984/9/35/010.
[21] R.F. Li, S.Q. Wu, Y. Yang, Z.Z. Zhu, Structural and electronic properties of Li-Ion battery cathode material FeF_3, J. Phys. Chem. C 114 (2010) 16813–16817, https://doi.org/10.1021/jp1050518.
[22] Z. Li, B. Wang, C. Li, J. Liu, W. Zhang, Hydrogen-bonding-mediated structural stability and electrochemical performance of iron fluoride cathode materials, J. Mater. Chem. A 3 (2015) 16222–16228, https://doi.org/10.1039/C5TA03327F.
[23] R. Shirakami, H. Ueda, H.O. Jeschke, H. Nakano, S. Kobayashi, A. Matsuo, T. Sakai, N. Katayama, H. Sawa, K. Kindo, C. Michioka, K. Yoshimura, Two magnetization plateaus in the kagome fluoride $Cs_2LiTi_3F_{12}$, Phys. Rev. B 100 (2019), 174401, https://doi.org/10.1103/PhysRevB.100.174401.
[24] M. Vlasse, F. Menil, C. Moriliere, J.M. Dance, A. Tressaud, J. Portier, Etude cristallographique et par effet Mössbauer du fluorure ferrimagnétique $Na_5Fe_3F_{14}\gamma$, J. Solid State Chem. 17 (1976) 291–298, https://doi.org/10.1016/0022-4596(76)90134-1.
[25] B.H. Toby, R factors in Rietveld analysis: how good is good enough? Powder Diffr. 21 (2006) 67–70, https://doi.org/10.1154/1.2179804.
[26] A.R. Patterson, R. Elizalde-Segovia, K.E. Wyckoff, A. Zohar, P.P. Ding, W. M. Turner, K.R. Poeppelmeier, S.R. Narayan, R.J. Clément, R. Seshadri, K. J. Griffith, Rapid and reversible lithium insertion in the Wadsley–roth-derived phase $NaNb_3O_{33}$, Chem. Mater. 35 (2023) 6364–6373, https://doi.org/10.1021/acs.chemmater.3c01066.
[27] D. Chen, J. Jie, M. Weng, S. Li, D. Chen, F. Pan, L.W. Wang, High throughput identification of Li ion diffusion pathways in typical solid state electrolytes and electrode materials by BV-Ewald method, J. Mater. Chem. A 7 (2019) 1300–1306, https://doi.org/10.1039/C8TA09345H.
[28] W.H. Ryu, H. Wilson, S. Sohn, J. Li, X. Tong, E. Shaulsky, J. Schroers, M. Elimelech, A.D. Taylor, Heterogeneous WS_x/WO_3 thorn-bush nanofiber electrodes for sodium-ion batteries, ACS Nano 10 (2016) 3257–3266, https://doi.org/10.1021/acsnano.5b06538.
[29] F. Bonino, S. Brutti, M. Piana, S. Natale, B. Scrosati, L. Gherghel, K. Müllen, Structural and electrochemical studies of a hexaphenylbenzene pyrolysed soft carbon as anode material in lithium batteries, Electrochim. Acta 51 (2006) 3407–3412, https://doi.org/10.1016/j.electacta.2005.09.036.
[30] H. Abdurehman Tariq, U. Nisar, J. James Abraham, Z. Ahmad, S. AlQaradawi, R. Kahraman, R.A. Shakoor, TiO_2 encrusted MXene as a High-Performance anode material for Li-ion batteries, Appl. Surf. Sci. 583 (2022), 152441, https://doi.org/10.1016/j.apsusc.2022.152441.
[31] P. Liu, J. Han, K. Zhu, Z. Dong, L. Jiao, Heterostructure $SnSe_2$/ZnSe@PDA nanobox for stable and highly efficient sodium-ion storage, Adv. Energy Mater. 10 (2020), 2000741, https://doi.org/10.1002/aenm.202000741.
[32] C. Jo, Y. Park, J. Jeong, K.T. Lee, J. Lee, Structural effect on electrochemical performance of ordered porous carbon electrodes for Na-Ion batteries, ACS Appl. Mater. Interfaces 7 (2015) 11748–11754, https://doi.org/10.1021/acsami.5b03186.
[33] Z. Jian, B. Zhao, P. Liu, F. Li, M. Zheng, M. Chen, Y. Shi, H. Zhou, Fe_2O_3 nanocrystals anchored onto graphene nanosheets as the anode material for low-cost sodium-ion batteries,, Chem. Commun. 50 (2014) 1215–1217, https://doi.org/10.1039/C3CC47977C.
[34] E. Bekaert, P. Balaya, S. Murugavel, J. Maier, M. Ménétrier, ^{6}Li MAS NMR investigation of electrochemical lithiation of RuO_2 : evidence for an interfacial storage mechanism, Chem. Mater 21 (2009) 856–861, https://doi.org/10.1021/cm8028005.
[35] L. Li, H. Jiang, N. Xu, X. Lian, H. Huang, H. Geng, S. Peng, Stable bismuth phosphosulfide nanoparticle encapsulation into hollow multi-channel carbon nanofibers toward high performance sodium storage, J. Mater. Chem. A 9 (2021) 17336–17343, https://doi.org/10.1039/D1TA05432E.
[36] S. López-Moreno, A.H. Romero, J. Mejía-López, A. Muñoz, I.V. Roshchin, First-principles study of electronic, vibrational, elastic, and magnetic properties of FeF_2 as a function of pressure, Phys. Rev. B 85 (2012), 134110, https://doi.org/10.1103/PhysRevB.85.134110.
[37] F.L. Bernal, K.V. Yusenko, J. Sottmann, C. Drathen, J. Guignard, O.M. Løvvik, W. A. Crichton, S. Margadonna, Perovskite to postperovskite transition in $NaFeF_3$, Inorg. Chem. 53 (2014) 12205–12214, https://doi.org/10.1021/ic502224y.
[38] U.K. Dey, N. Barman, S. Ghosh, S. Sarkar, S.C. Peter, P. Senguttuvan, Topochemical bottom-Up synthesis of 2D- and 3D-sodium iron fluoride frameworks, Chem. Mater. 31 (2019) 295–299, https://doi.org/10.1021/acs.chemmater.8b04010.
[39] J.H. Yu, C.H. Jo, H.J. Kim, S.T. Myung, Promising sodium storage of bismuthinite by conversion chemistry, Energy Storage Mater. 38 (2021) 241–248, https://doi.org/10.1016/j.ensm.2021.03.009.
[40] Q. Zhao, F.K. Butt, M. Yang, Z. Guo, X. Yao, M.J.M. Zapata, Y. Zhu, X. Ma, C. Cao, Tuning oxygen redox chemistry of P2-type manganese-based oxide cathode via dual Cu and Co substitution for sodium-ion batteries, Energy Storage Mater. 41 (2021) 581–587, https://doi.org/10.1016/j.ensm.2021.06.029.
[41] H. Wang, M. Gu, J. Jiang, C. Lai, X. Ai, An O3-type $NaNi_{0.5}Mn_{0.3}Ti_{0.2}O_2$ compound as new cathode material for room-temperature sodium-ion batteries, J. Power Sources 327 (2016) 653–657, https://doi.org/10.1016/j.jpowsour.2016.07.109.
[42] H. Wang, Y. Xiao, C. Sun, C. Lai, X. Ai, A type of sodium-ion full-cell with a layered $NaNi_{0.5}Ti_{0.5}O_2$ cathode and a pre-sodiated hard carbon anode, RSC Adv. 5 (2015) 106519–106522, https://doi.org/10.1039/C5RA21235A.
[43] B. Peng, Z. Sun, L. Zhao, J. Li, G. Zhang, Dual-manipulation on P2-$Na_{0.67}Ni_{0.33}Mn_{0.67}O_2$ layered cathode toward sodium-ion full cell with record operating voltage beyond 3.5V, Energy Storage Mater. 35 (2021) 620–629, https://doi.org/10.1016/j.ensm.2020.11.037.
[44] S.M. Oh, S.T. Myung, J.Y. Hwang, B. Scrosati, K. Amine, Y.K. Sun, High capacity O3-type $Na[Li_{0.05}(Ni_{0.25}Fe_{0.25}Mn_{0.5})_{0.95}]O_2$ cathode for sodium ion batteries, Chem. Mater. 26 (2014) 6165–6171, https://doi.org/10.1021/cm502481b.
[45] C. Yang, Y. Zhang, J. Bai, P. Tong, J. Lin, H. Tong, L. Zhang, W. Wen, X. Zhang, Y. Sun, Isotropic low thermal expansion over a wide temperature range in $Ti_{1-x}Zr_xF_{3+x}$ ($0.1 \leq x \leq 0.5$) solid solutions, Inorg. Chem. 57 (2018) 14396–14400, https://doi.org/10.1021/acs.inorgchem.8b02593.
[46] C. Yang, Y. Zhang, J. Bai, B. Qu, P. Tong, M. Wang, J. Lin, R. Zhang, H. Tong, Y. Wu, W. Song, Y. Sun, Crossover of thermal expansion from positive to negative by removing the excess fluorines in cubic ReO_3-type $TiZrF_{7-x}$, J. Mater. Chem. C 6 (2018) 5148–5152, https://doi.org/10.1039/C7TC04875K.
[47] M.C. Biesinger, L.W.M. Lau, A.R. Gerson, R.S.C. Smart, Resolving surface chemical states in XPS analysis of first row transition metals, oxides and hydroxides: *sc*, Ti, V, Cu and Zn, Appl. Surf. Sci. 257 (2010) 887–898, https://doi.org/10.1016/j.apsusc.2010.07.086.
[48] F. Zou, G.H. Lee, J. Zhang, V. Wing-hei Lau, J.J. Lee, Y.L. Yang, T.Y. Jeon, J. Zhang, J.B. Kim, K.W. Nam, Y.M. Kang, Steric modulation of $Na_2Ti_2O_3(SiO_4)\cdot 2H_2O$ toward highly reversible Na ion intercalation/deintercalation for Na ion batteries, Chem. Eng. J. 431 (2022) 1–7, https://doi.org/10.1016/j.cej.2021.133245.
[49] H. Pan, X. Lu, X. Yu, Y.S. Hu, H. Li, X.Q. Yang, L. Chen, Sodium storage and transport properties in layered $Na_2Ti_3O_7$ for room-temperature sodium-ion batteries, Adv. Energy Mater. 3 (2013) 1186–1194, https://doi.org/10.1002/aenm.201300139.
[50] Y. Dong, Z.S. Wu, S. Zheng, X. Wang, J. Qin, S. Wang, X. Shi, X. Bao, Ti_3C_2 MXene-derived sodium/potassium titanate nanoribbons for high-performance sodium/potassium ion batteries with enhanced capacities, ACS Nano 11 (2017) 4792–4800, https://doi.org/10.1021/acsnano.7b01165.
[51] Q. Lai, J. Mu, Z. Liu, L. Zhao, X. Gao, D. Yang, H. Chen, W. Luo, Tunnel-Type $Na_2Ti_6O_{13}$ @Carbon nanowires as anode materials for low-temperature sodium-ion batteries, Batter. Supercaps 6 (2023), https://doi.org/10.1002/batt.202200549.

[52] J. Tan, L. Liu, S. Guo, H. Hu, Z. Yan, Q. Zhou, Z. Huang, H. Shu, X. Yang, X. Wang, The electrochemical performance and mechanism of cobalt (II) fluoride as anode material for lithium and sodium ion batteries, Electrochim. Acta 168 (2015) 225–233, https://doi.org/10.1016/j.electacta.2015.04.029.

[53] Y. Huang, R. Ding, D. Ying, T. Yan, Y. Huang, C. Tan, X. Sun, E. Liu, Perovskite fluoride KMF_3 (M = Ni or Co)@reduced graphene oxide anode for Na-based dual-ion batteries, J. Alloys Compd. 891 (2022), 161905, https://doi.org/10.1016/j.jallcom.2021.161905.

[54] F. Yang, R. Ding, Z. Jia, W. Yu, Y. Li, A. Wang, M. Liu, J. Xie, M. Yan, Q. Fang, Y. Zhang, X. Sun, E. Liu, High specific energy and power sodium-based dual-ion supercabatteries by pseudocapacitive Ni-Zn-Mn ternary perovskite fluorides@reduced graphene oxides anodes with conversion-alloying-intercalation triple mechanisms, Energy Storage Mater. 53 (2022) 222–237, https://doi.org/10.1016/j.ensm.2022.08.049.

[55] L.T. López Ch, A. Medina, F. Jaramillo, J.A. Calderón, P. Lavela, J.L. Tirado, New insights on the reaction mechanism and charge contribution of $NaNiF_3$ perovskite as an anode for sodium-ion batteries, Electrochim. Acta 453 (2023), 142341, https://doi.org/10.1016/j.electacta.2023.142341.

[56] D. Puthusseri, M. Wahid, S. Ogale, Conversion-type anode materials for alkali-ion batteries: state of the art and possible research directions, ACS Omega 3 (2018) 4591–4601, https://doi.org/10.1021/acsomega.8b00188.

[57] W. Wei, S. Yang, H. Zhou, I. Lieberwirth, X. Feng, K. Müllen, 3D graphene foams cross-linked with pre-encapsulated Fe_3O_4 nanospheres for enhanced lithium storage, Adv. Mater. 25 (2013) 2909–2914, https://doi.org/10.1002/adma.201300445.

[58] Y. Lu, L. Yu, X.W. (David) Lou, Nanostructured conversion-type anode materials for advanced lithium-ion batteries, Chem 4 (2018) 972–996, https://doi.org/10.1016/j.chempr.2018.01.003.